Smart Agricultural Technology 14 (2026) 102304

Contents lists available at ScienceDirect

Smart Agricultural Technology

journal homepage: www.journals.elsevier.com/smart-agricultural-technology

A novel disease sensitive index (DSI) for monitoring early maize leaf disease using PROSPECT-D and LESS models

Yali Bai [a,b,c,d], Chenwei Nie [a,b,c], Jianbo Qi [e], Shuaibing Liu [a,b,c], Xun Yu [a,b,c], Xiao Jia [a,b,c], Qingzhi Liu [d], Bedir Tekinerdogan [d], Yang Song [f,*], Xiuliang Jin [a,b,*]

[a] Institute of Crop Science, Chinese Academy of Agricultural Sciences, Beijing 100081, China
[b] State Key Laboratory of Crop Gene Resources and Breeding, Beijing 100081, China
[c] National Nanfan Research Institute (Sanya), Chinese Academy of Agricultural Sciences, Sanya 572024, China
[d] Information Technology Group, Wageningen University & Research, Wageningen, 6708PB, the Netherlands
[e] Center for GeoData and Analysis, State Key Laboratory of Remote Sensing Science, Faculty of Geographical Science, Beijing Normal University, Beijing 100875, China
[f] School of Advanced Agricultural Sciences, University of Science and Technology Beijing, Beijing 100096, China

ARTICLE INFO

Keywords:
Maize disease
Multispectral sensor
Prospect-D
Less
Precision agriculture

ABSTRACT

Monitoring crop diseases on a large scale with non-destructive remote sensing technology is a promising approach to mitigating their impacts. However, monitoring early maize leaf diseases at canopy scales is still challenging. In this study, we introduce the Disease Sensitive Index (DSI), a novel disease index specifically designed to capture subtle physiological changes during early infection stages. Early leaf diseases predominantly cause changes in leaf pigments associated with photosynthesis, with a minimal impact on plant structure. Here, we analyzed the effects of leaf pigments and canopy structure on canopy spectral reflectance using PROSPECT-D and LESS models and found that the red-edge band (717 ± 5 nm) and green band (560 ± 10 nm) were more sensitive to leaf pigments than to canopy structure. By leveraging these bands, we presented the DSI. Our results demonstrated that the DSI was extremely statistically significant in differentiating rust severity, especially between low disease severity ($p < 0.001$). Furthermore, the DSI showed improved performance when quantifying the disease index (DI) across different years and sites ($R^2 = 0.69$ in 2021; $R^2 = 0.62$ in 2022). The time-series response patterns of vegetation indices (VIs) indicated that the DSI can detect disease onset as early as 10 days after infection (DAI 10). Furthermore, incorporating the DSI improved the machine learning model performance, consistently ranking as the most important predictor in feature importance analysis. Our findings highlight the potential of the DSI for monitoring early maize disease in precision agriculture.

1. Introduction

Maize serves as a significant staple crop, livestock feed, and ethanol fuel source worldwide [1]. However, the increased frequency of disease outbreaks in maize is a crucial reason for the reductions both in crop yield and quality [2]. Common leaf diseases in maize include maize rust and leaf spot. Infected leaves appear as small yellow spots at first, and then the spots gradually rise to form spore piles. These spore piles are mainly round or oval, golden or light brown in color, and scattered on the leaves' upper surface. As the disease becomes more serious, plant leaves fade from green to yellow and appear to senesce early [3]. Pathogen-infected crops show more changes in functional characteristics, such as biochemical composition and physical structure, than healthy plants [4,5]. Among these, leaves' anthocyanin (Anth), chlorophyll (C_{ab}), and carotenoid (C_{ar}) content are effective indicators for disease monitoring [6].

Traditional methods for monitoring maize disease rely on field visual inspection, which is laborious and limited by subjective experience [7]. Furthermore, it should be noted that by the time visual symptoms appear, significant crop damage has often already occurred, leading to high economic costs for the farmer. The primary goal of predictive modeling, therefore, is to detect disease in the pre-symptomatic stage to allow for the application of preventive treatments. Consequently, developing an objective and accurate approach to early monitoring of

* Corresponding authors.
E-mail addresses: songyang@ustb.edu.cn (Y. Song), jinxiuliang@caas.cn (X. Jin).

https://doi.org/10.1016/j.atech.2026.102304
Received 21 February 2026; Received in revised form 18 April 2026; Accepted 12 June 2026
Available online 13 June 2026

maize diseases at canopy scales is critical.

To achieve large-scale, non-destructive monitoring, remote sensing techniques have been widely adopted [8,9,5]. Recently, intelligent monitoring and data-driven frameworks have achieved remarkable success across complex engineering fields. For example, artificial neural networks (ANNs) and hybrid machine learning models are now used to optimize wireless power transmission systems [10], detect real-time faults in photovoltaic modules [11], forecast short-term electricity demand [12], and improve fault-tolerant regulation [13] in motor drives. While these purely data-driven algorithms excel at extracting non-linear features, remote sensing models for crops require a stricter grounding in physiological reality. Because remote sensing data provides optical estimations rather than absolute ground truth, relying solely on visual features often results in models with limited predictive power. An effective plant disease monitoring framework must therefore integrate four critical components: selecting disease-sensitive features, establishing predictive models, evaluating accuracy, and conducting physiological validation. Among these components, feature selection serves as the foundation, directly determining the initial accuracy of the monitoring models [14,15]. Various vegetation indices (VIs) are common remote sensing features used in monitoring plant disease. For instance, the chlorophyll/carotenoid index (CCI), simple ratio pigment index (SRPI), and health-index (HI) have been identified as sensitive features for distinguishing between rice leaf blast and healthy leaves across different years [15]. Additionally, the normalized difference vegetation index (NDVI) has been extensively utilized in identifying diseases [16,17]. However, due to limitations in disease specificity identification of these common VIs [18–20], there has been a pressing need to propose VIs based on disease-specific spectral information.

Disease-specific VIs are often proposed following a spectral response analysis of specific disease lesions. For example, Ren et al., [21] developed the yellow rust spore index (YRSI) using fungal spore information on leaves to identify yellow rust. The powdery mildew-index, yellow rust-index, and aphids-index were developed by Huang et al., [18] to identify and monitor different winter wheat diseases. Mahlein et al., [20] identified disease specific single wavelengths from sugar beet leaves and developed the leaf spot index, sugar beet rust index, and powdery mildew index to monitor and identify sugar beet diseases. However, these VIs are calculated based on hyperspectral data's narrow spectral reflectance and are less effective for low-cost multispectral data [22]. Additionally, these specific disease indices, which are derived from leaf spectral data, do not consider the structural parameters of plants, leading to a decrease in accuracy during canopy monitoring tasks [23].

Previous studies highlighted that photosynthetic pigments, detectable through remote sensing techniques, act as physiological indicators for monitoring the early responses of plants to various stressors, as reviewed by Hernandez-Clemente et al., [6]. Among these pigments, chlorophyll is the primary pigment group. Building on this foundation, we hypothesize that an index sensitive to chlorophyll variations yet effective against changes in plant structure will be effective for the early detection of plant diseases. To test this hypothesis, our research employed simulations derived from radiative transfer models to replicate changes in pigment and structural parameters triggered by maize leaf diseases (Fig. 4a). The simulations used the latest version of the PROSPECT model, PROSPECT-D [24], and the large-scale remote sensing data and image simulation framework, LESS [25]. PROSPECT-D generates leaf spectra by considering various biochemical components, while LESS incorporates these leaf spectra into different maize planting scenarios to generate simulated canopy spectra. In the LESS, varying the plant spacing (PS) is used to represent different planting scenarios. These variations result in diverse leaf area index values and distinct clumping patterns within the canopy. Therefore, the objectives of this study were to (i) understand responses of spectral reflectance and VIs to changes in biochemical and PS through radiative transfer modeling; (ii) develop a multispectral index (i.e., DSI developed in this study) that is sensitive to chlorophyll changes but resistant to PS; and (iii) validate the performance of the proposed DSI for maize disease monitoring.

2. Materials

2.1. Experimental site

Our study sites located in Xinxiang City, China, are characterized by a warm temperate continental monsoon climate with hot summers and cold winters (113°47′E, 35°10′N, Fig. 1). This region is predominantly a maize-growing area of China, typically cultivated in May and harvested in October. To evaluate the effectiveness of the proposed Disease Sensitive Index (DSI), four experimental sites (A, B, C, and D) were established across two growing seasons (2021 and 2022). These sites focused on two prevalent maize leaf diseases: maize rust and leaf spot. Specifically, Sites A, C, and D were dedicated to leaf spot monitoring via artificial inoculation, while Site B leveraged the natural occurrence of maize rust.

Sites A and B were planted in Xinxiang on May 30, 2021. Site A consisted of 492 plots (1.25 m × 1.80 m each), with each plot dedicated to a unique maize genotype. The planting configuration utilized a constant row spacing of 60 cm and an intra-row PS of 18.5 cm. This site underwent treatment with a leaf spot bacterial solution on the evening of August 2, 2021. Site B was designed to examine the impact of canopy structure on disease monitoring. It comprised four sections (2475.2 m^2 each), each representing a different planting density. Maintaining a constant inter-row spacing of 60 cm, these sections featured PS of 37.0 cm, 27.8 cm, 22.2 cm, and 18.5 cm, respectively. Each section was further divided into 14 plots, each plot hosting a different maize variety. These varieties exhibited varying levels of resistance to maize rust, introducing different disease severities across the study site. Given that maize rust is a recurring disease in the study region, the rust naturally occurred.

Sites C and D, located in Yuanyang, with the same planting geometry as Site A were planted on May 30, 2022. Site C was organized into 120 rows of 3 m, with every 20rows forming a plot containing a unique genotype. A subset of these plots was selected as infected areas that received treatment with the leaf spot bacterial solution on August 2, 2022, marked in red on the overview map of site C. We identified healthy areas (uninfected areas, yellow masked areas), which are equal in number and size to the infected areas. These, infected and healthy areas were intermingled and distributed at intervals to minimize the impact of pathogen transmission. Site D had 1031 rows of 3 m, each considered an individual plot. All plots received treatment with the leaf spot bacterial solution on August 2, 2022. In managing fields, we adhered to fertilizer application and irrigation practices guided by the expertise of local agricultural professionals and established standards. This approach aimed to maintain a balanced supply of water and nutrients, minimizing their potential influence on the prevalence of maize diseases.

2.2. Field survey

Our field surveys adhered to the survey standard of maize rust by China's Ministry of Agriculture (NY/T 1248.14–2021) and China's national standard (NY/T 1248.1–2006), titled technical specification for identification of maize resistance to leaf spot disease. This approach is organized into two primary segments: leaf-level assessment and canopy-level assessment. Initially, it involves quantifying the leaf disease (n) level based on the area of a leaf affected by the target disease. Subsequently, a canopy disease index (DI) is computed, incorporating the disease levels of leaves from all randomly sampled plants.

The practical procedure was divided into four main stages: sample collection, expert analysis, DI calculation, and resistance/disease severity assessment (Fig. 2). Initially, we documented images of maize leaves above, at, and below ear level. Following this, three independent experts categorized each leaf into a class based on visual assessments of

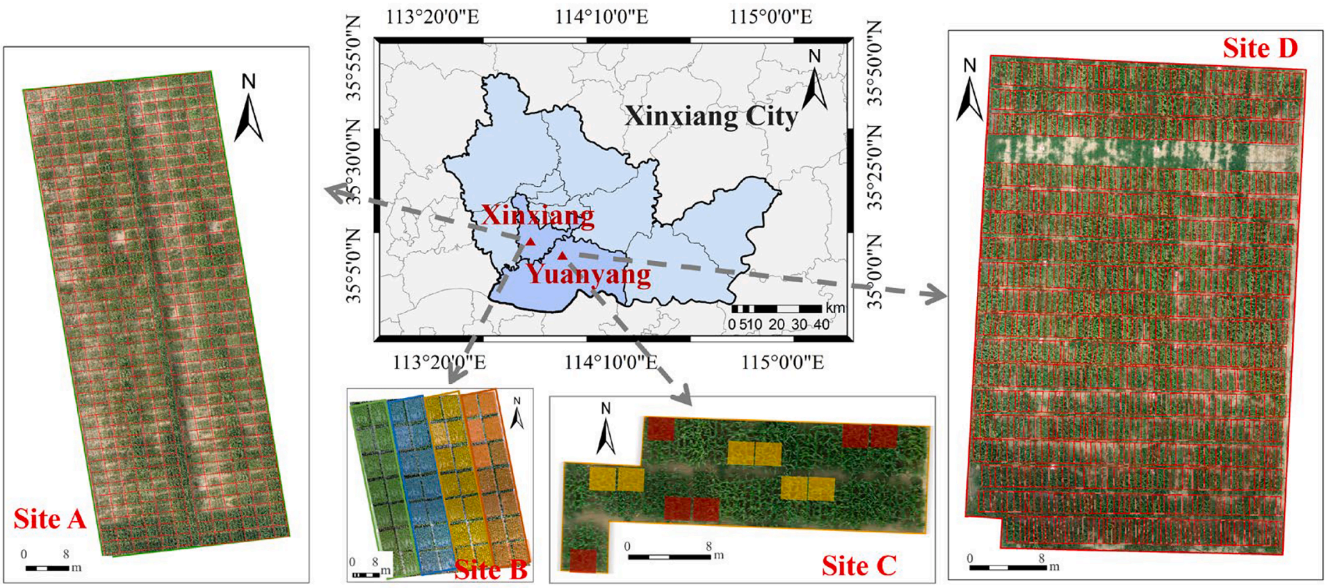

Fig. 1. Layout of field experiments at two locations (Xinxiang and Yuanyang) in 2021 and 2022. The upper center figure shows the geographic location of experimental sites. Site A (left) and B (lower left) in Xinxiang in 2021. Green, blue, yellow, and orange in site B denote intra-row plant spacings (PS) of 37.0 cm, 27.8 cm, 22.2 cm, and 18.5 cm, respectively. Site C (lower right) and D in Yuanyang in 2022. The red mask in site C presents infected areas, and the yellow mask shows healthy areas.

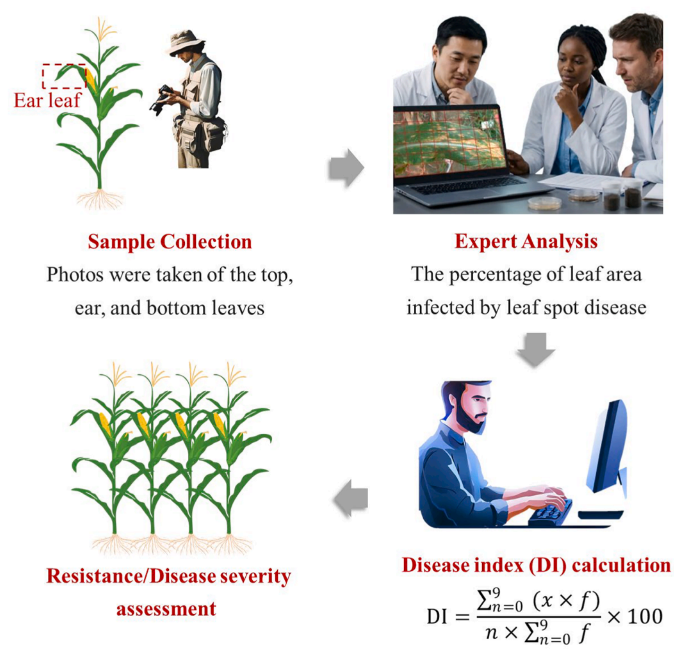

Fig. 2. Flow chart of maize field leaf disease survey. x is the class determined by the proportion of a leaf affected by disease spots. The values for x are defined as 0, 1, 3, 5, 7, and 9, representing respective disease areas of 0%, 0%–5%, 6%–25%, 26%–50%, 51%–75%, and 76%–100% on a leaf; f is the total number of leaves of each class; n refers to the highest leaf disease severity (in this paper, n = 9). The resistance or disease severity can be assessed in various application scenarios based on the disease index (DI).

disease spot coverage. To minimize subjectivity and ensure repeatability in visual assessments, we implemented a grid-masking technique in which a 5 × 10 transparent grid was overlaid on sampled leaves to accurately quantify the percentage of the lesion area. After the visual classification of leaves, the DI was calculated to quantify the overall disease severity at the plot scale, with values ranging from 0% to 100% according to the following equation:

$$DI(\%) = \sum_{i=0}^{n} (X_i \cdot S_i) \Bigg/ \sum_{i=0}^{n} (X_i \cdot S_{\max}) \times 100 \quad (1)$$

Where, S_i represents the degree of disease severity, taking values of 0, 1, 3, 5, 7, and 9, which correspond to lesion coverage ranges of 0%, 1%–5%, 6%–25%, 26%–50%, 51%–75%, and 76%–100%, respectively; and S_{max} is the highest degree of disease severity, which in this study is 9; i denotes the degree of disease severity (0–n); X_i is the number of leaves assigned to severity class i.

Finally, we assessed resistance or disease severity based on various application scenarios. We classified maize resistance into two categories: resistant (DI ranging from 0 to 30%) and susceptible (DI ranging from 31 to 100%) according to maize breeding program. Similarly, we categorized the disease severity in maize plots into three levels: low (DS 1, DI of 0–30%), medium (DS 2, DI of 31–60%), and high (DS 3, DI of 61–100%).

At sites A and D, genotype resistance to leaf spot was assessed. Field surveys at these sites were conducted on August 21, 2021, and August 24, 2022, respectively. Site A hosted 492 genotypes, comprising 311 susceptible and 181 resistant genotypes. Conversely, site D hosted 1013 genotypes, including 483 susceptible and 530 resistant genotypes. At site B, the disease severity of maize rust was evaluated. Field surveys were conducted on August 27, September 3, and September 8, 2021. A total of 168 samples (56 plots × 3 surveys) were included in this study, among which there were 12 for DS 1, 31 for DS 2, and 125 for DS 3. Since each plot contains numerous homogenous observations (pixels), we subdivided DS 1 plots into twelve equal parts and DS 2 plots into four equal parts, inspired by the data processing methodologies described by Damm et al., [26]. This approach aimed to capture the intra-plot variability of disease symptoms and balance the sample distribution for model training and validation. As a result, the final sample distribution for this study was adjusted to 120 samples for DS 1, 124 samples for DS 2, and 125 samples for DS 3. In site C, visual inspections were conducted every two days after the onset of the disease infection. These visual inspections revealed that areas of the disease lesions continued to expand in infected areas and remained unaffected by the disease in healthy areas.

2.3. Multispectral imagery

The details of our multispectral images obtained from flight missions are presented in Table 1. For sites B and D, the image capture time coincided with the field survey dates. For sites A and C, images were collected sequentially, allowing for a time-lapse view of disease progression.

High-resolution multispectral images were taken under clear skies using a RedEdge-MX mounted on a multi-rotor UAV (DJI-M600Pro, SZ DJI Technology Co., Ltd., Shenzhen, China) at the height of 30 m above ground during the local time window of 10:00–14:00. Both lateral and forward overlaps were set at 80%. The RedEdge-MX is a 5-band multispectral camera, including blue band (B: 465–485 nm), green band (G: 550–570 nm), red band (R: 663–673 nm), red-edge band (*Re*: 712–722 nm), and near-infrared band (NIR: 820–860 nm). A standard Micasense panel, captured at the beginning and end of each flight, was used to convert raw images into reflectance images.

2.4. Simulation data

This paper used radiative transfer models to estimate the effects of structural parameters and leaf pigment contents on spectral reflectance and VIs. The application of radiative transfer models aimed to understand the responses of spectral reflectance and VIs to biochemical and structural changes [27]. Understanding these responses is crucial for developing a new canopy index sensitive to target biochemical changes during early maize leaf disease occurrence.

The canopy reflectance of a maize field was simulated by coupling the leaf-level PROSPECT-D [24] model with the canopy-level LESS model [25]. PROSPECT-D is a radiative transfer model for broadleaf crops that can simulate the reflectance of leaves based on information on leaf pigments such as Anth, C_{ab}, and C_{ar} [24]. The LESS model is a realistic three-dimensional (3D) canopy radiation transfer model based on a ray tracing algorithm that accurately describes interactions between solar radiation and heterogeneous surfaces [25]. In LESS, crop planting scenes can be described by adjusting different planting distances to describe various planting scenarios in a realistic maize field (Fig. 3). The combination of PROSPECT-D and LESS model was used to evaluate the effects of PS and leaf biochemical parameters (C_{ab}, C_{ar}, and Anth) on spectral reflectance and VIs. The ranges for these inputs were established based on the LOPEX and ANGERS databases [24], the LESS database, technical sensor data, and field measurements. A detailed breakdown of these input variables and their specific sources is provided in Table 2 and Table S1. Row-direction effects were neglected based on our specific UAV flight window and nadir viewing geometry, which minimizes the impact of canopy anisotropy. A total of 4032 synthetic canopy images were generated. The mean reflectance of these images was used to analyze responses of spectral reflectance to the changes in biochemical and structural parameters. .

Table 1
Overview of research sites and data collection schedule.

Site	Location	Disease Type	Study Year	Survey Timing	Survey Outputs	Image Collection Schedule
A	Xinxiang	Leaf spot	2021	Aug. 21	Resistance	July 31, Aug. 4, Aug. 14, Aug. 21, Sep. 1 (DAI −2, 4, 12, 19, 30)
B	Xinxiang	Rust	2021	Aug. 2, Sep. 3, Sep. 8	DI/DS	Aug. 27, Sep. 3, Sep. 8
C	Yuanyang	Leaf spot	2022	N/A	N/A	Aug. 2, Aug. 4, Aug. 6, Aug. 8, Aug. 10, Aug. 12, Aug. 14, Aug. 17, Aug. 24, Aug. 26, Sep. 1 (DAI 0, 2, 4, 6, 8, 10, 12, 15, 22, 24, 30)
D	Yuanyang	Leaf spot	2022	Aug. 24	DI/ Resistance	Aug. 24

DI: disease index; DS: disease severity; DAI: day after infections; N/A: not applicable. Each site or output serves as an independent dataset for evaluating the performance of the DSI across various scenarios.

3. Methods

The experimental design of this study is illustrated in Fig. 4. The following subsections detail the generation of synthetic data using the PROSPECT-D and LESS models (Section 2.4), the derivation of the DSI (Sections 3.2 and 3.3), and the evaluation of its performance using both simulated datasets and UAV-acquired imagery (Sections 3.4 and 3.5).

3.1. Analysis of spectral and pigment dynamics after disease infection

This section aims to analyze the dynamics of spectral and pigment changes following disease infection in maize leaves, focusing on early detection and monitoring. Disease in the early stage typically exhibits constitutive changes among leaf photosynthetic pigment pools [28,5], with increasing disease severity over time causing variations in plant structure [7]. However, in the practical field, plant structures are inconsistent due to variations in PS and cultivars [29]. Therefore, features sensitive to pigments but insensitive to PS have the potential for early disease monitoring [30].

To validate this viewpoint, we collected time series leaf spectral data after maize leaf spot infection. An ASD Field Spec PRO 4 (Analytical spectral devices, Inc., boulder, colorado, U.S.) was equipped with a leaf clip to measure the leaf reflectance. We identified and marked 84 infected leaves for spectral measurements. We obtained reflectance spectra for each leaf at three different points on the adaxial surface (1/3, 1/2, and 2/3 of the distance from the base, respectively). An average reflectance was calculated by the spectra collected from each leaf to minimize random measurement errors. It should be noted that we only utilized 20 leaves of all the measured leaves for further analysis. That is because these leaves demonstrated a consistent increase in the infected area and consequently showed a rise in disease severity.

The pigment was quantified by inverting the PROSPECT-D model. The C_{ab} was specifically analyzed due to its obvious response in the multispectral sensors used in this study, as compared to C_{ar} and Anth. The input variables for this model were estimated based on datasets about leaf optical properties [31] and prior studies [32]. We utilized the iterative optimization method, the fminsearch function in Matlab, to invert the PROSPECT-D model. This method was employed to pinpoint the best-simulated spectra from each model, identified as those with the lowest root mean square error (RMSE) value, following the approach of previous research [33].

The collected leaf spectra showed an obvious pattern in infected leaves on various days after infection (Fig. 5a, taking a selected leaf as an example). At the early stage of the disease, significant spectral alterations mainly occur in the visible region, especially the primary absorption band for pigments [34]. Additionally, as disease severity increases, C_{ab} retrieved by PROSPECT-D revealed a consistent reduction (Fig. 5b). This finding confirmed that PROSPECT-D model-based C_{ab} is consistent with the process of disease infection.

3.2. Responses of spectral reflectance to pigments content and PS

The average reflectance of images simulated by the radiative transfer model demonstrated responses of multispectral reflectance to pigments content and PS (Fig. 6). The reflectance of band B is lightly affected by

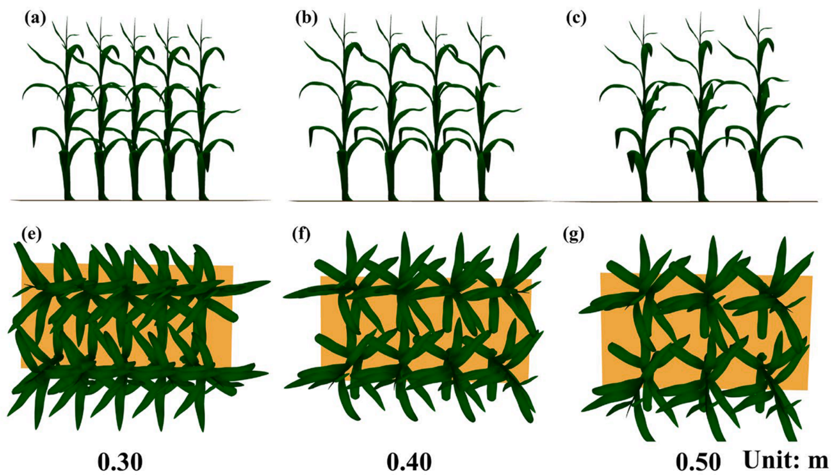

Fig. 3. 3D scenes generated with LESS to simulate variations in plant spacing (PS). The top row corresponds to a horizontal view, while the bottom row corresponds to a top view. (a) and (e) depict a planting spacing of 0.30 m, (b) and (f) illustrate a spacing of 0.40 m, as well as (c) and (g) show a spacing of 0.50 m.

Table 2
The inputs of PROSPECT-D and LESS.

Variable	Units	Acronym	Values	Steps	Source
		PROSPECT-D			
Leaf structural parameter	-	N	1.5	-	[24]
Dry matter content	g/cm^2	C_m	0.012	-	
Brown pigment content	-	-	0	-	
Carotenoids content	μg/cm^2	C_{ar}	0–60	10	
Chlorophyll content	μg/cm^2	C_{ab}	15–70	5	
Anthocyanin content	μg/cm^2	Anth	0–5	1	
Water equivalent thickness	Cm	C_w	0.015	-	
		LESS			
Plant spacing	M	PS	0.2–0.55	0.05	Field measurements

Note: Other inputs in the LESS model are shown in Table S1 in the supplemental information.

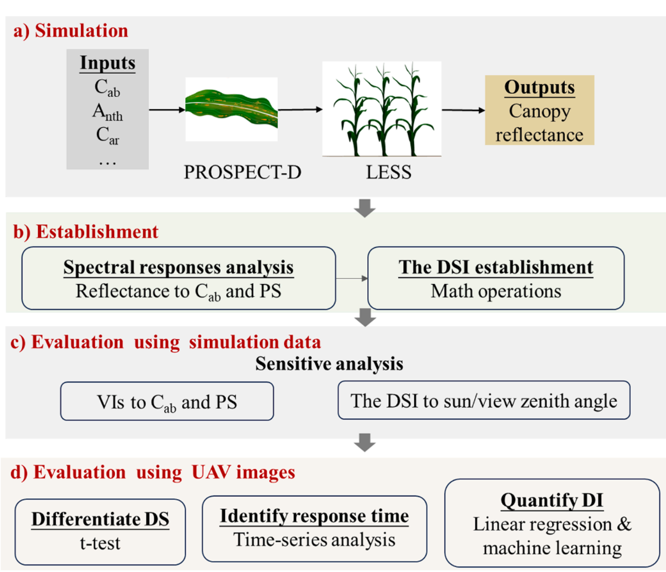

Fig. 4. Flowchart of the experimental design. PS: plant spacing, DI: disease index; DS: disease severity.

PS. The G varies with different levels of C_{ab} and Anth. The R is primarily influenced by PS, with a slight sensitivity to C_{ab}. The *Re* is primarily influenced by C_{ab} and has a minor sensitivity to PS. The NIR varies with different levels of PS. Therefore, the *Re* and G are selected to be combined with other bands to create a new index that is sensitive to pigments but not to PS.

3.3. Establishment of the DSI

Building upon our spectral response analysis in Section 3.2, we identified *Re* and G reflectance as being particularly sensitive to variations in C_{ab} and Anth while exhibiting minimal sensitivity to PS. These findings facilitated the creation of the DSI. The DSI encompasses the following three critical components:

(1) Normalized pigment sensitivity component. We crafted a normalized index using *Re* plus G with NIR. The NIR is known for distinguishing between vegetative and non-vegetative surfaces [35,36]. Normalization mitigates radiometric differences across remote sensing images, rendering data from diverse temporal and sensor sources comparable for analysis [37,38]. Since NIR is sensitive to PS, the normalized component simultaneously accounts for pigment and PS variations.
(2) PS sensitivity reduction component. To mitigate the DSI's sensitivity to PS, we included the B, which has demonstrated a similar range sensitivity to PS as the *Re*. These spectral characteristics lead to the ratio formulation $R_B/(R_G + R_{\mathrm{Re}})$, where the similar trends in both the numerator (B) and denominator (*Re*) could approximately cancel out during calculation, thus reducing the influence of PS. Due to the saturation resistance of *Re* and G, this formulation has a wider C_{ab} sensitivity range [39].
(3) Gain factor (K). To normalize the DSI values within a practical range, primarily between 0 and 1 for vegetative areas, we introduced a gain factor, K. Based on the range of simulation results, we set K = 10 for our study. This scaling ensures the DSI is dimensionless and comparable across different datasets.

The DSI is constructed as follows:

$$DSI = \mathrm{K} \times \frac{R_{\mathrm{NIR}} - R_{\mathrm{G}} - R_{\mathrm{Re}}}{R_{\mathrm{NIR}} + R_{\mathrm{G}} + R_{\mathrm{Re}}} \times \frac{R_{\mathrm{B}}}{R_{\mathrm{G}} + R_{\mathrm{Re}}} \quad (2)$$

3.4. Evaluations of VIs in various disease monitoring scenarios

To evaluate the performance of the DSI in maize disease monitoring, we compared it to VIs sensitive to C_{ab} and those used in previous plant disease monitoring studies (Table 3). Our comparison focused on three aspects: the ability of these indices to differentiate between different rust severity, the correlation with DI, and the response time after disease

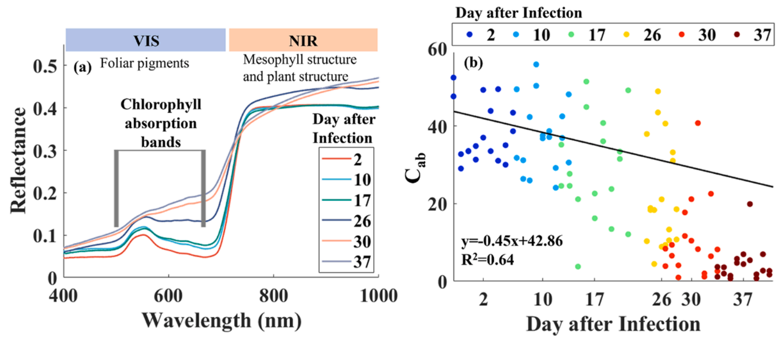

Fig. 5. Changes of measured spectrum (a) and model-based chlorophyll content (b) (C_{ab} [μg/cm²]) from an infected leaf on various days after infection.

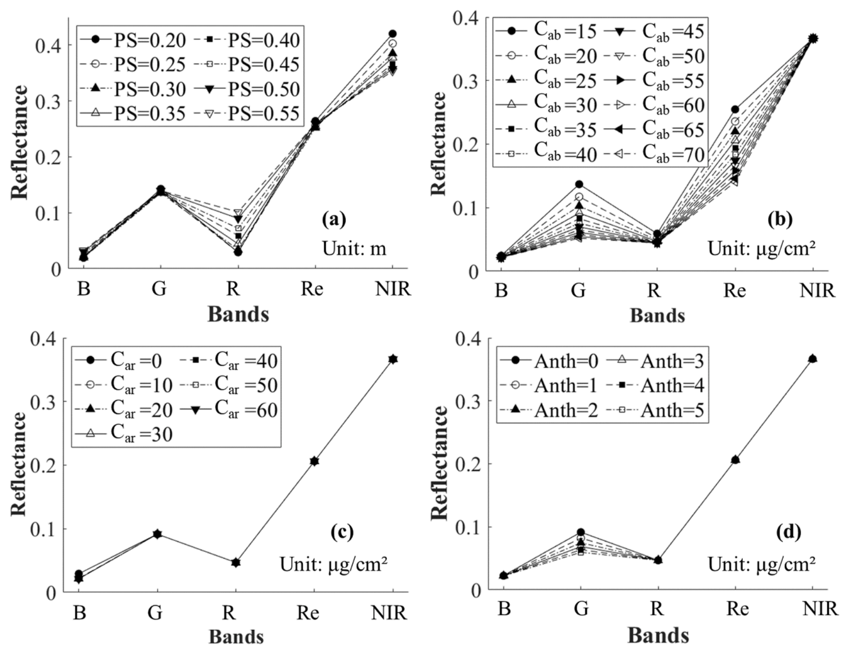

Fig. 6. Simulations by coupling PROSPECT-D and LESS model to evaluate the effects of plant spacing (PS), chlorophyll content (C_{ab}), carotenoids content (C_{ar}), and anthocyanin content (Anth) on the reflectance used in this study. B, G, R, *Re*, and NIR are blue band (465–485 nm), green band (550–570 nm), red band (663–673 nm), red-edge band (712–722 nm), and near-infrared band (820–860 nm), respectively.

infection (Table 4).

In the first aspect, the *t*-test with the *p*-value was used to determine significant differences between different maize rust severity, including not considered statistically significant ($p > 0.05$, ns), statistically significant ($p < 0.05$, *), very statistically significant ($p < 0.01$, **), and extremely statistically significant ($p < 0.001$, ***).

In the second aspect, simple linear regression models were employed to evaluate the performances of VIs in quantifying DI in maize leaf diseases. The dataset was initially divided into a training set (80%) and a testing set (20%). We determined the linear equations for each VI and DI pair within the training set. The significance of the regression variables was interpreted by *p*-values. The performances of these linear equations were then assessed using three metrics in the testing set: coefficient of determination (R^2), root mean square error (RMSE), and relative root mean square error (rRMSE).

In the third aspect, time-series analysis was used to evaluate the response time of VIs to maize diseases. This involved a normalization approach that accounted for canopy structure effects on the hyperspectral features. We calculated the difference between feature values on the day after infection and the day before infection. The time series changes in each feature were then analyzed. To determine the impact of leaf disease on maize plants, we utilized statistical measures: 95% confidence intervals based on a z-distribution and effect size using Cohen's d. An effect size larger than 0.8 indicates a substantial difference between healthy and infected plants. The start of consecutive substantial differences (|effect sizes| $\geq$ 0.8) marks the VI's initial response to the disease.

3.5. Machine learning and feature importance

To evaluate the effectiveness of the DSI as an input feature for machine learning models, we employed three regression algorithms to estimate the DI: Random Forest (RF), Gradient-Boosting Decision Tree (GBDT), and Support Vector Regression (SVR). For model training, each dataset was randomly divided into a training set (80%) and a testing set (20%). A grid search combined with a 5-times repeated 10-fold cross-validation was applied to the training set to optimize hyperparameters. Model performance on the testing set was evaluated using R^2, RMSE, and mean absolute error (MAE). We compared model accuracies under two input scenarios: Case 1, utilizing traditional VIs only; and Case 2, combining traditional VIs with the DSI. Furthermore, we utilized the SHapley Additive exPlanations (SHAP) method [40] to interpret the RF models and assess the relative importance of each VI.

Table 3
Vegetation indices (VIs) used in this paper.

VIs	Abbreviation	Equal	Reference
VIs sensitive to C_{ab}			
Disease sensitive index	DSI	$10[(R_{NIR} - R_G - R_{Re})/(R_{NIR} + R_G + R_{Re})][R_B/(R_G + R_{Re})]$	This paper-
Red-edge normalized difference vegetation index	$NDVI_{re}$	$R_{NIR} - [R_{Re}/(R_{NIR} + R_{Re})]$	[41]
Red-edge chlorophyll index	CI_{re}	$R_{NIR}/R_{Re} - 1$	[42]
MERIS terrestrial chlorophyll index	MTCI	$(R_{NIR} - R_{Re})/(R_{Re} - R_R)$	[43]
Transformed chlorophyll absorption in reflectance index	TCARI	$3[(R_{Re} - R_R) - 0.2(R_{Re} - R_G)/(R_{Re}/R_R)]$	[44]
Datt 99	Datt99	$(R_{NIR} - R_{Re})/(R_{NIR} - R_R)$	[45]
TCARI/optimized soil-adjusted vegetation index	TCARI/ OSAVI	$TCARI/[(1 + 0.16)(R_{NIR} - R_R)/(R_{NIR} + R_R + 0.16)]$	[46]
Red reflectance of the vegetation	RED_v	$R_R \times [(R_{NIR} - R_R)/(R_{NIR} + R_R)]^2$	[47]
VIs used for monitoring plant disease in previous papers			
Chlorophyll/carotenoid index	CCI	$(R_G - R_R)/(R_G + R_R)$	[48]
Simple ratio pigment index	SRPI	R_B/R_R	[49]
Health-index	HI	$(R_G - R_{Re})/(R_G + R_{Re}) - (0.5 \times R_{Re})$	[20]
Normalized difference vegetation index	NDVI	$(R_{NIR} - R_R)/(R_{NIR} + R_R)$	[50]

Table 4
Summary of statistical methods and outcomes.

Aim	Statistical Methods	Description	Outcome/Metric
Differentiation of rust severity	*t*-test	Used to determine significant differences in maize rust severity	not considered statistically significant (ns): $p > 0.05$ statistically significant (*): $p < 0.05$ very statistically significant (**): $p < 0.01$ extremely statistically significant (***): $p < 0.001$
Quantifying DI in maize leaf diseases	- Simple linear regression - Machine learning	Evaluated the performance of VIs in quantifying DI	Linear equations for each VI and DI pair Significance of regression variables: *p*-values Coefficient of determination: R^2 Root mean square error: RMSE Relative root mean square error: rRMSE mean absolute error: MAE
Response time to disease infection	Time-series analysis	Assessed the response time of VIs to maize leaf diseases	95% confidence intervals: z-distribution Effect size: Cohen's d

4. Results

4.1. Sensitive analysis of VIs using simulated data

4.1.1. Sensitivity of VIs to c_{ab} and PS

The VIs calculated from the average reflectance of synthetic images displayed the response of these indices to C_{ab} and PS (Fig. 7). For indices sensitive to C_{ab}, the DSI, MTCI, and Datt99 showed a strong correlation with C_{ab}, while their sensitivity to PS alterations was notably subdued. In contrast, $NDVI_{re}$, CI_{re}, TCARI, TCARI/OSAVI, and RED_v responded to both PS and C_{ab}. Meanwhile, VIs used in previous plant disease monitoring studies, such as CCI, SRPI, and NDVI, were responsive to both PS and C_{ab}, while HI displayed insensitivity to PS at C_{ab} levels under 35 μg/cm^2.

4.1.2. Sensitivity of the DSI to sun/view zenith angle

The changes of solar zenith angle (SZA) and view zenith angle (VZA) induce little difference in the DSI, as shown in Fig. 8. The curves for VZA and SZA were relatively flat, indicating that the changes in these parameters have a minor impact on the DSI. In contrast, the curve for C_{ab} showed a more pronounced trend, signifying a higher sensitivity of the DSI to the change of C_{ab}.

4.2. Performances of VIs in differentiating DS

The ability of VIs to differentiate disease severity was scrutinized using a *t*-test (Fig. 9). All chlorophyll-sensitive VIs showed an extremely significant capacity to identify high disease severity when comparing DS 1 to DS 3 and DS 2 to DS 3. However, these VIs showed different patterns in discerning between DS 1 and DS 2. Specifically, $NDVI_{re}$ and TCARI/OSAVI did not show a significant difference with a *p*-value greater than 0.05, TCARI and RED_v were statistically significant ($p < 0.05$), and the DSI, CI_{re}, MTCI, and Datt99 were found to be extremely statistically significant ($p < 0.001$). Contrastingly, VIs previously validated as sensitive to other diseases manifested varying capacities in distinguishing the severity of rust disease. These VIs showed an extremely significant capacity to identify DS 2 when compared with DS 1 and DS 3. However, these VIs showed different patterns in discerning between DS 1 and DS 2. In specific, NDVI did not show a significant difference; CCI was statistically significant ($p < 0.05$), and SRPI and HI were found to be extremely statistically significant ($p < 0.001$).

4.3. Performances of VIs in quantifying DI

The relationships between VIs and DI in maize fields infected with rust are shown in Fig. 10. The performances of chlorophyll-related VIs outperformed other indices used in previous disease monitoring studies. The R^2 for chlorophyll-related VIs ranged between 0.38 and 0.69, with RMSE values from 0.13 to 0.22. In contrast, indices validated for sensitivity to other diseases showed a broader range of R^2 from 0.11 to 0.63, with RMSE values stretching from 0.16 to 0.24. DSI, MTCI, and SRPI demonstrated superior performance with lower RMSE and rRMSE alongside higher R^2 values among the tested indices. Specifically, DSI achieved the highest accuracy (R^2=0.69, RMSE=0.13).

The relationships between VIs and DI in fields infected with maize leaf spot were presented in Fig. 11. Similar to the findings in rust infection fields, chlorophyll-related VIs were more effective than disease sensitive indices used in previous studies. The R^2 values for chlorophyll-related VIs ranged from 0.25 to 0.62. Other disease sensitive indices ranged more variably in effectiveness, with R^2 values from 0.07 to 0.58. Among them, the DSI attained the highest accuracy with the highest R^2 value (R^2=0.62), followed by SRPI (R^2=0.58).

4.4. Response time of VIs to maize leaf disease

The analysis of temporal multispectral imagery to differentiate

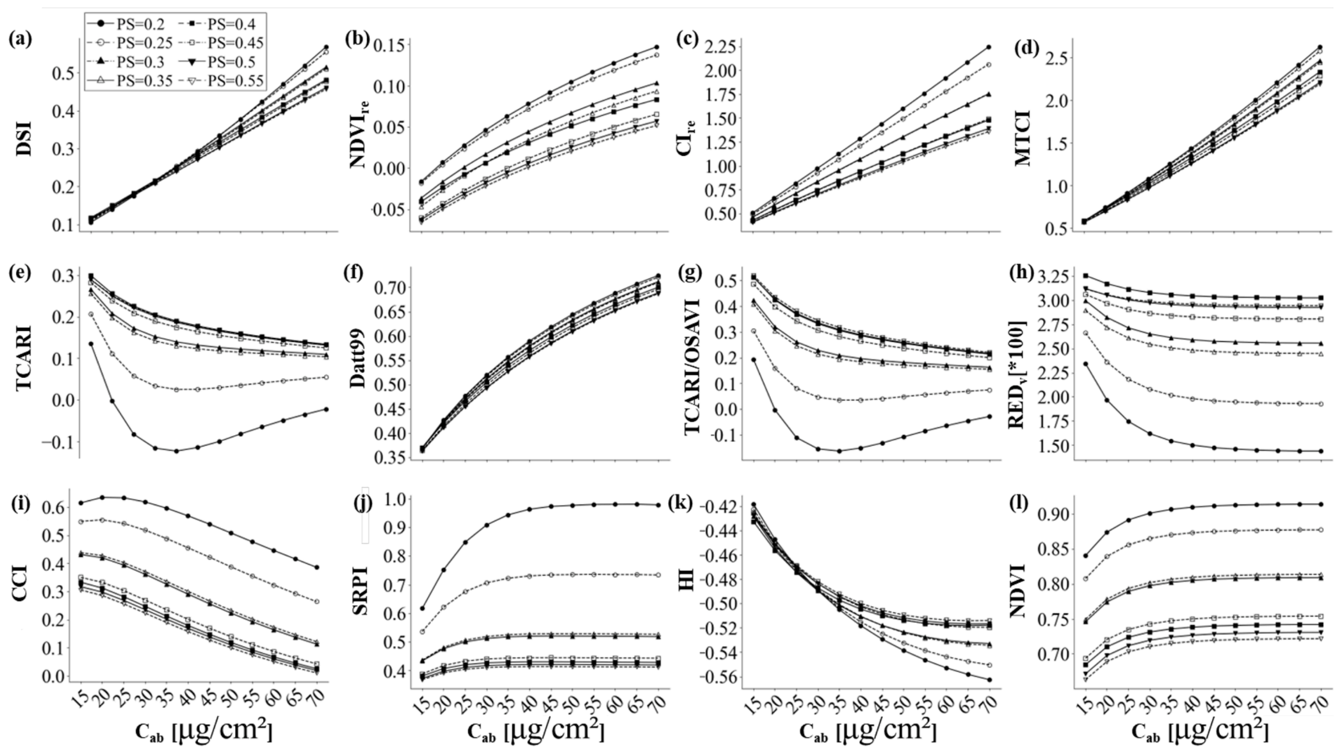

Fig. 7. Sensitivity of vegetation indices (VIs) to plant spacing (PS) and Chlorophyll content (C_{ab}) using simulations based on PROSPECT-D and LESS model. (a)–(h) represent VIs sensitivities to C_{ab}, including DSI, $NDVI_{re}$, CI_{re}, MTCI, TCARI, Datt99, TCARI/OSAVI, and RED_v. (i)–(l) show VIs used in previous plant disease monitoring studies, including CCI, SRPI, HI, and NDVI.

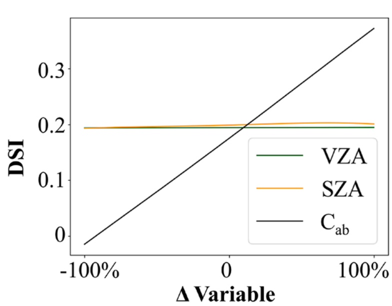

Fig. 8. Sensitivity of the DSI to variations in different parameters. View zenith angle (VZA) variation range: 0°–20°, reference value: 10°; solar zenith angle (SZA) variation range: 20°–60°, reference value: 40°; Chlorophyll content (C_{ab}) variation range: 10–70 μg/cm^2, reference value: 35 μg/cm^2.

resistance and susceptibility of leaf spot disease in site A revealed distinct patterns (Fig. 12). Only the DSI demonstrated a consistently substantial difference (|effect sizes| ≥ 0.8) from DAI 12. TCARI, RED_v, CCI, and NDVI showed a consistent substantial difference from DAI 19. Datt99, and SRPI exhibited substantial differences only on individual days, failing to show a continuous trend. Other indices did not show substantial differences in the period of observation.

The analysis of temporal multispectral imagery to differentiate infected and healthy areas to leaf spot disease in site C was shown in Fig. 13. DSI, TCARI, CCI, SRPI, and NDVI presented substantial differences over three or more consecutive time points. The DSI exhibited the earliest response to infection from DAI 10, followed by CCI from DAI 12, and NDVI from DAI 15. TCARI began to respond to infection from DAI 22, while SRPI responded from DAI 24. Other indices did not show continuously substantial differences within the period of observations.

4.5. Impact of DSI on machine learning model performance

The performances of the machine learning algorithms for estimating the DI in the 2021 Site B and 2022 Site D datasets are presented in Table 5. For all three models, the inclusion of the DSI (Case 2) resulted in higher R^2 and lower RMSE and MAE values compared to Case 1. For example, using the RF model, the testing R^2 increased from 0.65 to 0.71 in Site B, and from 0.60 to 0.70 in Site D.

The relative importance of the VIs was evaluated using SHAP values derived from the RF models (Fig. 14). The SHAP summary plots indicate that the DSI had the highest overall importance score in regressing the DI across both datasets, followed by SRPI. The color distribution in the SHAP plots shows that high DSI feature values (red dots) correspond to negative SHAP values, indicating a negative correlation with the predicted DI. This observation is consistent with the univariate regression results in Section 4.3. While the importance rankings of the other VIs varied between the two datasets, the DSI maintained a stable contribution to the model output.

5. Discussion

5.1. Consistency of measured and simulated reflectance

The reflectance of soil, healthy canopy, low leaf disease severity canopy, and high leaf disease severity canopy from remote sensing imagery was visually interpreted (Fig. S1). The canopy reflectance of low and high disease severity at G, R, and *Re* ranges was higher than that of a healthy maize canopy, and this symptom was attributed to the degradation of C_{ab} caused by maize leaf disease. This characteristic is also generally presented at an early stage of other diseases, such as rust in sugar beet [20], laurel wilt disease in avocado [51], and *Xylella fastidiosa* infection in olive [5]. At the NIR region, the canopy reflectance of the high severity canopy was slightly lower than that of the healthy and low severity canopies due to the significant reduction of green leaves. This

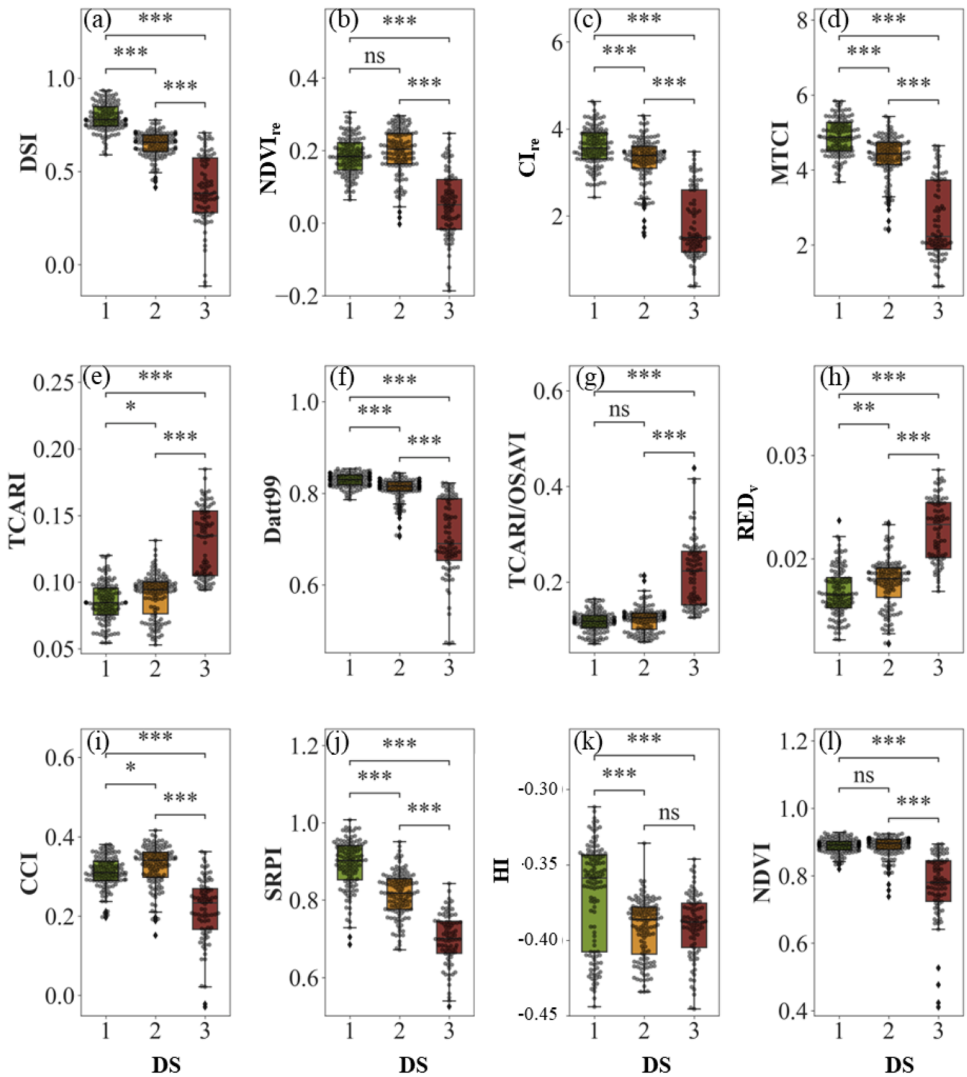

Fig. 9. Significant differences in vegetation indices (VIs) across various rust disease severity (DS): low (DS 1), medium (DS 2), and high (DS 3). (a)–(h): VIs sensitive to C_{ab}, including DSI, $NDVI_{re}$, CI_{re}, MTCI, TCARI, Datt99, TCARI/OSAVI, and RED_v. (i)–(l): VIs were used in previous plant disease monitoring studies, including CCI, SRPI, HI, and NDVI. Distinctions were made based on the p-value: not considered statistically significant ($p > 0.05$, ns), statistically significant ($p<0.05$, *), very statistically significant ($p<0.01$, **), and extremely statistically significant ($p<0.001$, ***).

characteristic was also observed in the canopy of rice blast [9] and *Xylella fastidiosa* infection in olive orchards [52]. These trends of spectral response were consistent with our simulated spectra and our hypothesis that the pigment changes happened in an early disease stage. As the disease progresses, the structural parameters of the crop begin to change. These results suggest that simulated spectra caused by pigment content variations can represent spectral changes caused by maize leaf disease, and it is feasible to construct a vegetation index using simulated spectra.

While these overall trends are consistent, it is crucial to acknowledge the inherent discrepancies between simulated and real-world canopy reflectance. For instance, rather than altering a single variable, disease infection triggers a synergy of physiological and structural changes that indirectly affect radiative transfer. Although using the PROSPECT-D and LESS models with evenly spaced parameters allows for rapid data generation without field measurements, this method fails to represent the full complexity of disease dynamics. Consequently, the gap between simulation and reality may limit the real-world robustness of the proposed index.

5.2. Interpretability of remote sensing features to biochemical and structural characteristics

To understand the way spectral reflectance and VIs respond to biochemical and structural characteristics, the performances of these remote sensing features were evaluated within the simulation dataset. This dataset was constructed by coupling PROSPECT-D and LESS models. Multispectral imagery with broadband has demonstrated an apparent capacity to reflect changes in C_{ab} and plant structure (i.e., modifications in leaf area index and fractional vegetation cover induced by variations in PS). Nevertheless, these reflectance measurements exhibit a weak sensitivity to changes in Anth and are insensitive to variations in C_{ar} levels. VIs developed for monitoring C_{ab} exhibited variability patterns upon various C_{ab} and PS. The DSI, in line with MTCI, and Datt99, has shown a pronounced sensitivity to C_{ab} while remaining relatively unaffected by alterations in PS. Additionally, the DSI was slightly affected by sun/view zenith angel compared to C_{ab}.

The degradation of plant pigments due to biotic stresses can cause green leaves to yellow and fade, and even result in the death of the entire plant when the leaf disease becomes high severity level. Simultaneously, various planting conditions and cultivars can also lead to differences in

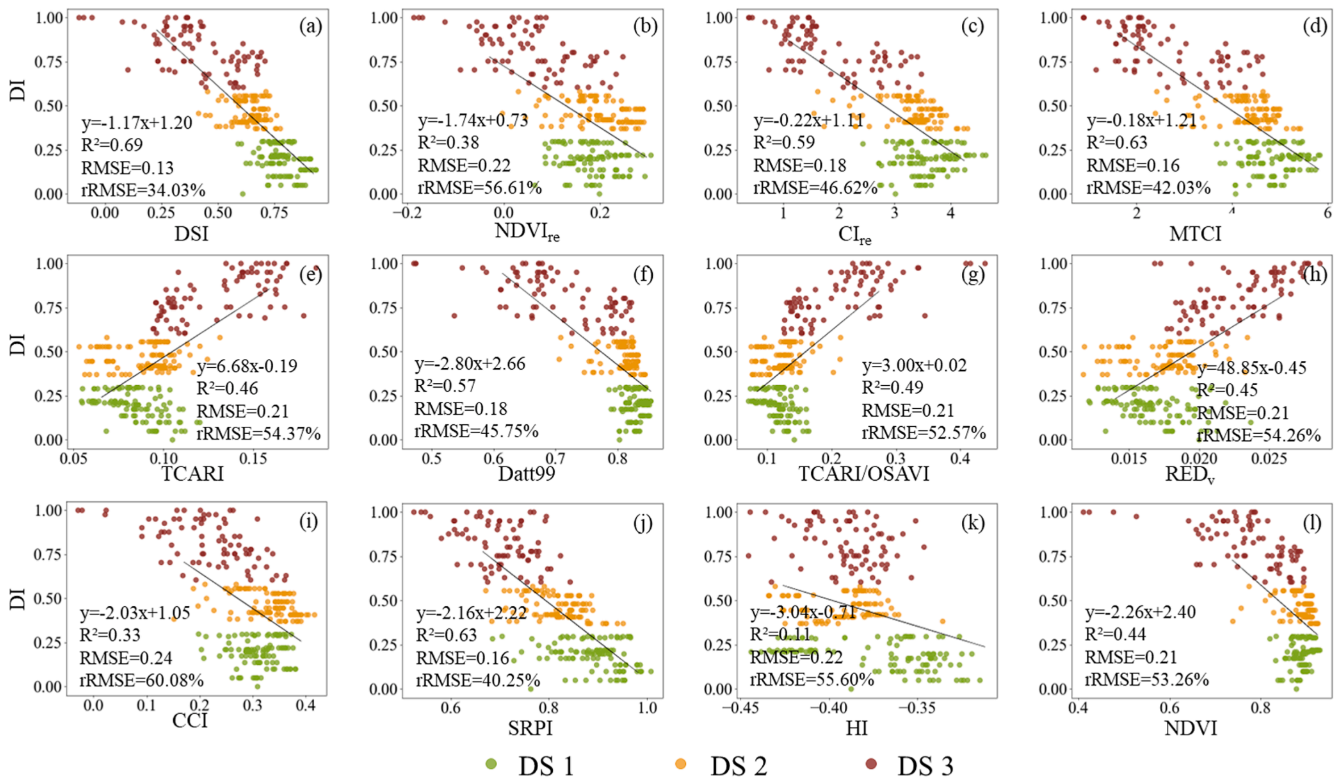

Fig. 10. Relationships between vegetation indices (VIs) and disease index (DI) in maize rust infected fields. The low (DS 1), medium (DS 2), and high (DS 3) severity of disease were represented in colors of green, yellow, and red, respectively. All regressions were statistically significant ($p < 0.05$).

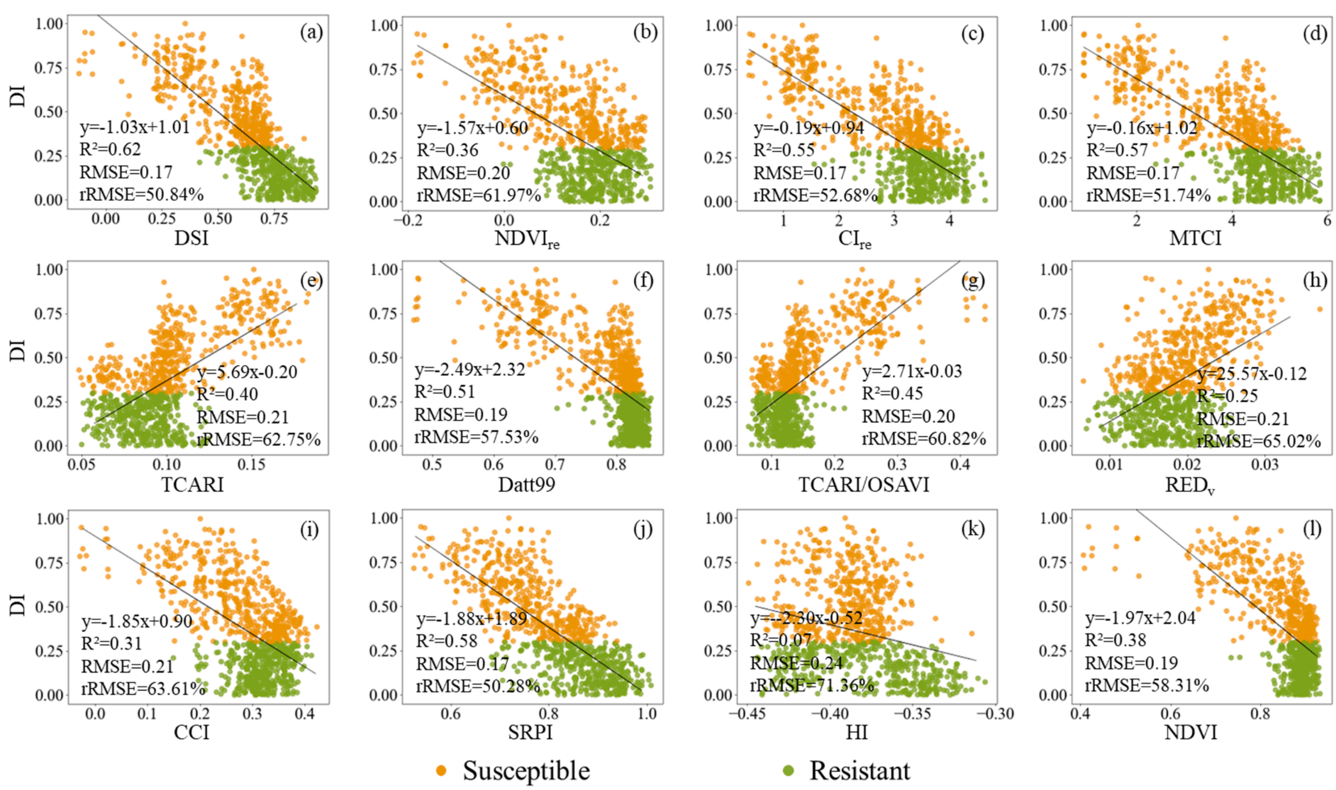

Fig. 11. Relationships between vegetation indices (VIs) and disease index (DI) in maize leaf spot infected fields. The resistant and susceptible genotypes were represented in green and yellow colors. All regressions were statistically significant ($p < 0.05$).

crop morphology and fractional vegetation cover. Therefore, it is crucial to identify features sensitive to pigments but not structure in monitoring

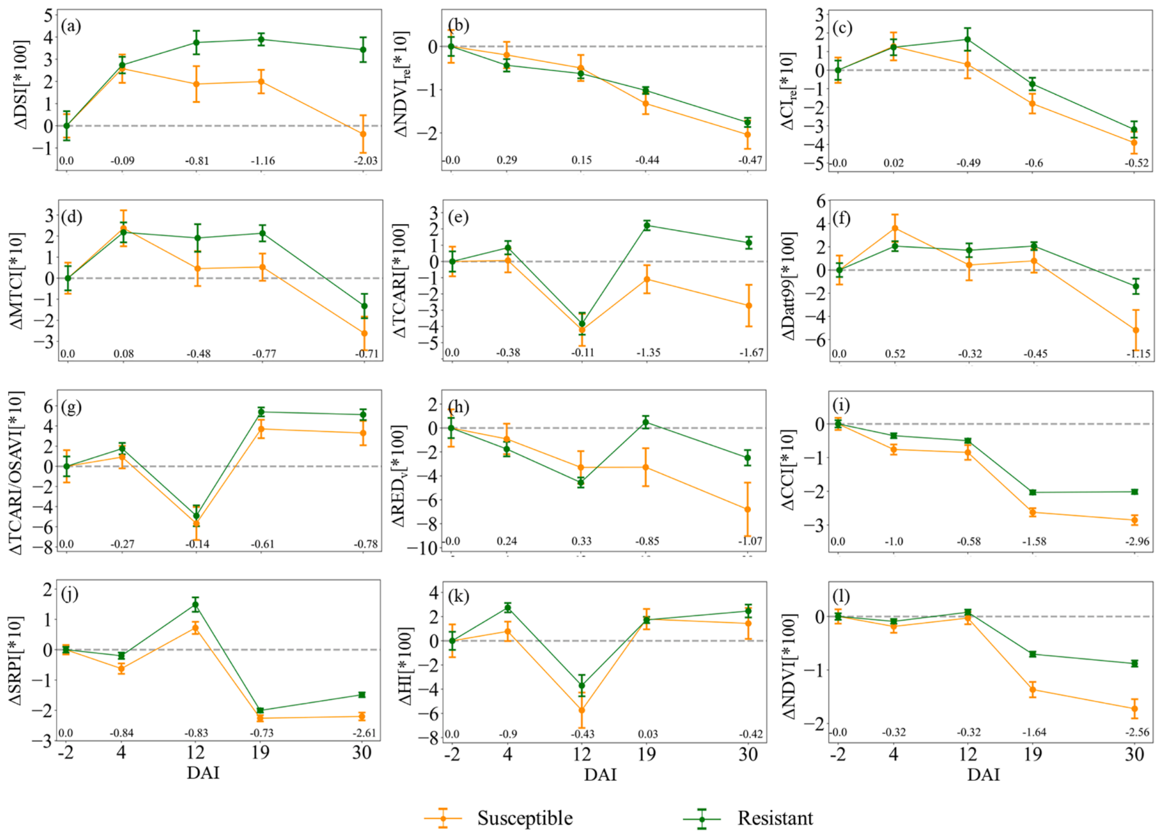

Fig. 12. Changes of vegetation indices (VIs) on different days after infection (DAIs) in maize leaf spot infected fields in 2021 (site A). Error bars represent the 95% confidence interval, and values represent the effect size using Cohen's d.

early disease.

5.3. Performance of the DSI in monitoring maize leaf disease

The effectiveness of the DSI is rooted in its design philosophy of physical decoupling. While traditional indices often struggle with canopy structural variations, the DSI was optimized to isolate pathological signals from structural noise. By minimizing sensitivity to plant spacing—a proxy for canopy coverage and soil background interference—the DSI ensures that spectral shifts primarily reflect the crop's physiological response rather than geometric interference. This decoupling mechanism is fundamental to the index's ability in disease monitoring.

Based on data gathered from four distinct experimental sites in two consecutive years (2021, 2022), our investigations into the performances of the DSI in monitoring maize leaf disease have yielded significant insights. Notably, the DSI has emerged as the most accurate tool in quantifying DI, showing the earliest substantial response to disease infection, appearing as early as DAI 12 in 2021 and DAI 10 in 2022. These findings strongly indicate the scalability and adaptability of the DSI across diverse environments, highlighting its potential for early-stage maize leaf disease monitoring.

Furthermore, our study has revealed promising results with DSI-like indices such as MTCI and Datt99, which show promising results in different disease monitoring scenarios. This effectiveness further solidifies that plant disease at an early stage is primarily marked by changes in C_{ab} levels. Meanwhile, chlorophyll-sensitive VIs show superior capability in disease monitoring applications compared to indices previously used for other disease monitoring. These findings underscore the potential of specific chlorophyll-related VIs for precise and reliable monitoring of maize leaf diseases at an early stage. Therefore, developing and utilizing an index sensitive to C_{ab} changes is advantageous for the early monitoring maize leaf disease.

The sensitive indices identified in previous disease monitoring studies showed poor sensitivity to maize leaf diseases in this study. These indices are usually derived from specific diseases in specific scenarios. The mechanisms of disease onset vary among different diseases, leading to poor transferability of indices between different diseases [53, 54].

Furthermore, incorporating the DSI as an input feature improved the regression accuracy of the evaluated machine learning models compared to relying solely on traditional VIs. The SHAP analysis revealed that the DSI consistently ranked high in feature importance across both datasets. This suggests that the DSI is an effective, physically interpretable feature for enhancing data-driven crop disease monitoring.

Our findings suggest that the DSI could serve as a stable and suitable solution for early maize rust and leaf spot monitoring. The DSI enhances its correlation with C_{ab} by utilizing *Re* reflectance in conjunction with G. This enhancement is crucial as C_{ab} is a key indicator of disease onset. Additionally, the negative correlation between G reflectance and Anth further augments the DSI's sensitivity to Anth. Anth has been widely acknowledged for revealing disease occurrence, even in its early or asymptomatic stages [17,14,5]. Therefore, leveraging these relationships makes the DSI an effective tool for pigment and disease detection.

5.4. Limitations and future work

The DSI is developed using commonly available broadband multispectral sensors, offering a cost-effective and simple solution for data acquisition and analysis in practical agricultural production. The ability of the DSI in monitoring early disease could guide precise pesticide application, reduce pesticide usage and enhance food quality. Additionally, distinguishing maize resistance can aid breeders in rapidly selecting target genotypes.

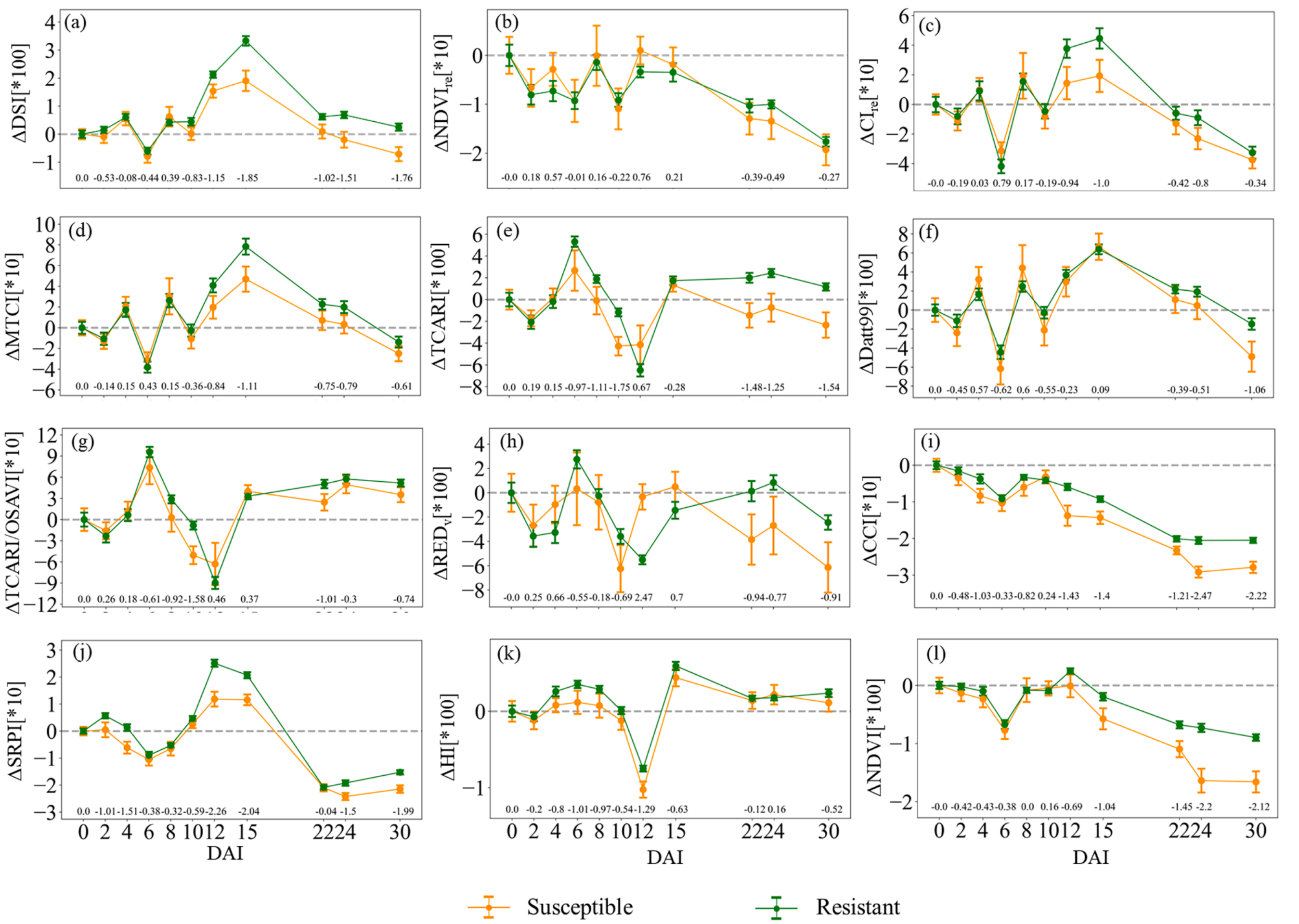

Fig. 13. Changes of vegetation indices (VIs) on different days after infection (DAIs) in maize leaf spot infected fields in 2022 (site C). Error bars represent the 95% confidence interval, and values represent the effect size using Cohen's d.

Table 5
Summary of machine learning model performance.

Year	Model	Case	Cross-validation set			Test set		
			R^2	RMSE	MAE	R^2	RMSE	MAE
2021	**RF**	Case1	0.72±0.06	0.11±0.02	0.08±0.01	0.65	0.15	0.10
Site B		Case2	**0.83±0.06**	0.11±0.02	0.08±0.01	**0.71**	0.15	0.10
	GBDT	Case1	0.71±0.05	0.13±0.01	0.09±0.01	0.61	0.15	0.10
		Case2	0.76±0.07	0.13±0.02	0.09±0.01	0.70	0.15	0.10
	SVR	Case1	0.71±0.05	0.12±0.02	0.09±0.01	0.63	0.15	0.11
		Case2	0.81±0.05	0.11±0.02	0.09±0.01	0.70	0.15	0.11
2023	**RF**	Case1	0.71±0.05	0.14±0.02	0.10±0.01	0.63	0.14	0.11
Site D		Case2	**0.80±0.04**	0.12±0.02	0.08±0.01	**0.70**	0.13	0.09
	GBDT	Case1	0.70±0.06	0.15±0.01	0.11±0.01	0.61	0.16	0.11
		Case2	0.78±0.05	0.13±0.01	0.09±0.01	0.69	0.14	0.10
	SVR	Case1	0.73±0.07	0.15±0.02	0.11±0.01	0.61	0.14	0.12
		Case2	0.79±0.06	0.13±0.02	0.09±0.01	0.67	0.14	0.10

However, we acknowledge that the current validation of the DSI remains geographically and biologically narrow. Although this study utilized data from four sites across two years, all experiments were conducted within a limited regional climate. This constrains the immediate generalizability of the proposed index. Crucially, this study has only tested the DSI in two mainstream maize diseases: rust and leaf spot. The feasibility of the DSI in other maize leaf diseases and crops remains unknown. For broader agricultural uses, the robustness of the DSI should be validated under different stress (such as water and nitrogen deficit) conditions across diverse climatic zones, a broader range of crop cultivars, and other disease types in the future. Moreover, our modeling assumptions simplified real canopy complexity. In this study, early disease was treated primarily as a pigment-change problem, and structural variability was represented mainly through PS in the LESS model. While effective for isolating the dominant baseline density effects, this approach oversimplifies real-world conditions where reflectance is simultaneously influenced by soil background variability, genotype-dependent architecture, and complex illumination effects. Future iterations of the DSI should incorporate more comprehensive plant architectures and dynamic soil reflectance within radiative transfer simulations to enhance robustness in highly heterogeneous fields. Finally, the DSI's sensitivity to pigments changes caused by early-stage

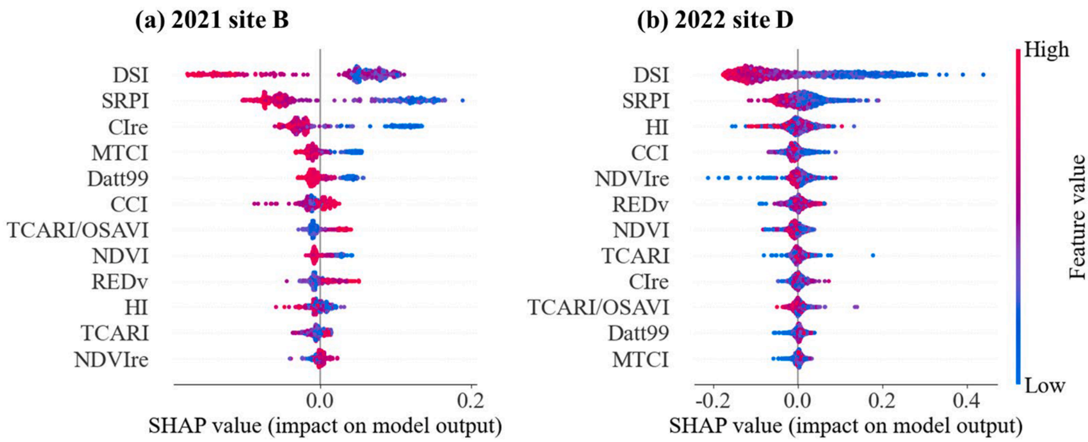

Fig. 14. SHAP summary plots of feature importance for DI estimation. Features are ranked by their overall contribution to the Random Forest model from top to bottom. Each point represents an individual sample, with the color indicating the feature value (red for high, blue for low).

leaf disease means it lacks disease specificity and cannot differentiate between diseases that cause similar pigment changes. Its broad-band properties also challenge capturing more spectral details, such as carotenoid changes, which provide chemical defenses against biological stress [55].

6. Conclusion

This study highlights the effectiveness of a chlorophyll-sensitive index in monitoring maize leaf diseases. The changes in spectral reflectance and VIs under varying pigment content and PS were successfully simulated by coupling PROSPECT-D and LESS models. The results show that *Re* and G bands were slightly affected by PS but were sensitive to leaf pigments. Therefore, the DSI was proposed, showing higher sensitivity to changing C_{ab} while less affected by alterations in PS and solar/view zenith angles within our simulated dataset. Further empirical evaluation of the DSI has been tailored for diverse disease monitoring scenarios. Statistically evidence ($p < 0.001$) supports the DSI's discriminative capability in distinguishing between low maize rust severity and medium. Compared with other VIs, the proposed DSI has shown a stronger relationship with the DI for rust infected field ($R^2 = 0.69$) and leaf spot infected field ($R^2 = 0.62$). Temporal analysis of multispectral imagery using the DSI consistently revealed significant differences at DAI 12 in differentiating resistant/susceptible and DAI 10 in differentiating infected/healthy areas in leaf spot disease infected field. These results support the use of DSI and canopy imagery for monitoring the onset of disease infection, and for facilitating decision-making about disease identification in breeding experiments and control measures on farms.

Ethical statement

This article does not contain any studies with human participants or animals performed by any of the authors.

CRediT authorship contribution statement

Yali Bai: Writing – review & editing, Writing – original draft, Visualization, Methodology, Formal analysis, Data curation, Conceptualization. **Chenwei Nie:** Writing – review & editing, Methodology. **Jianbo Qi:** Writing – review & editing, Methodology. **Shuaibing Liu:** Data curation. **Xun Yu:** Data curation. **Xiao Jia:** Data curation. **Qingzhi Liu:** Writing – review & editing, Supervision. **Bedir Tekinerdogan:** Writing – review & editing, Supervision. **Yang Song:** Writing – review & editing, Visualization. **Xiuliang Jin:** Writing – review & editing, Supervision, Funding acquisition.

Declaration of competing interest

The authors declare the following financial interests/personal relationships which may be considered as potential competing interests:

Xiuliang Jin reports financial support was provided by National Natural Science Foundation of China.

Acknowledgment

This research was supported by Nanfan special project, CAAS (YBXM2401, YBXM2402), National Natural Science Foundation of China (42071426) Research and application of key technologies of smart brain for farm decision-making platform (2021ZXJ05A03), the Agricultural Science and Technology Innovation Program of the Chinese Academy of Agricultural Sciences.

Supplementary materials

Supplementary material associated with this article can be found, in the online version, at doi:10.1016/j.atech.2026.102304.

Data availability

Data will be made available on request.

References

[1] P. Ranum, J.P. Pena-Rosas, M.N. Garcia-Casal, Global maize production, utilization, and consumption, Ann. N. Y. Acad. Sci. 1312 (2014) 105–112.
[2] S. Chakraborty, A.C. Newton, Climate change, plant diseases and food security: an overview, Plant Pathol. 60 (2011) 2–14.
[3] Q. Sun, L. Li, F. Guo, K. Zhang, J. Dong, Y. Luo, Z. Ma, Southern corn rust caused by Puccinia polysora Underw: a review, Phytopathol. Res. 3 (2021) 25.
[4] C.W. Ahrens, M.E. Andrew, R.A. Mazanec, K.X. Ruthrof, A. Challis, G. Hardy, M. Byrne, D.T. Tissue, P.D. Rymer, Plant functional traits differ in adaptability and are predicted to be differentially affected by climate change, Ecol. Evol. 10 (2020) 232–248.
[5] P.J. Zarco-Tejada, C. Camino, P.S.A. Beck, R. Calderon, A. Hornero, R. Hernandez-Clemente, T. Kattenborn, M. Montes-Borrego, L. Susca, M. Morelli, V. Gonzalez-Dugo, P.R.J. North, B.B. Landa, D. Boscia, M. Saponari, J.A. Navas-Cortes, Previsual symptoms of Xylella fastidiosa infection revealed in spectral plant-trait alterations, Nat. Plants. 4 (2018) 432–439.
[6] R. Hernandez-Clemente, A. Hornero, M. Mottus, J. Penuelas, V. Gonzalez-Dugo, J. C. Jimenez, L. Suarez, L. Alonso, P.J. Zarco-Tejada, Early diagnosis of vegetation health from high-resolution hyperspectral and thermal imagery: lessons learned from empirical relationships and radiative transfer modelling, Curr. For. Rep. 5 (2019) 169–183.
[7] K. Berger, M. Machwitz, M. Kycko, S.C. Kefauver, S. Van Wittenberghe, M. Gerhards, J. Verrelst, C. Atzberger, C. van der Tol, A. Damm, U. Rascher, I. Herrmann, V.S. Paz, S. Fahrner, R. Pieruschka, E. Prikaziuk, M.L. Buchaillot, A. Halabuk, M. Celesti, G. Koren, E.T. Gormus, M. Rossini, M. Foerster, B. Siegmann, A. Abdelbaki, G. Tagliabue, T. Hank, R. Darvishzadeh, H. Aasen,

M. Garcia, I. Pôças, S. Bandopadhyay, M. Sulis, E. Tomelleri, O. Rozenstein, L. Filchev, G. Stancile, M. Schlerf, Multi-sensor spectral synergies for crop stress detection and monitoring in the optical domain: a review, Remote Sens Env. 280 (2022) 113198.
[8] T. Poblete, C. Camino, P.S.A. Beck, A. Hornero, T. Kattenborn, M. Saponari, D. Boscia, J.A. Navas-Cortes, P.J. Zarco-Tejada, Detection of Xylella fastidiosa infection symptoms with airborne multispectral and thermal imagery: assessing bandset reduction performance from hyperspectral analysis, ISPRS. J. Photogramm. Remote Sens. 162 (2020) 27–40.
[9] L. Tian, Z. Wang, B. Xue, D. Li, H. Zheng, X. Yao, Y. Zhu, W. Cao, T. Cheng, A disease-specific spectral index tracks magnaporthe oryzae infection in paddy rice from ground to space, Remote Sens Env. 285 (2023) 113384.
[10] H. Uzel, Y. Özüpak, F. Alpsalaz, E. Aslan, Optimized ANN–RF hybrid model with optuna for fault detection and classification in power transmission systems, Sci. Rep. 16 (2025) 1495.
[11] Y. özüpak, Real-time detection of photovoltaic module faults using a hybrid machine learning model, Sol. Energy 302 (2025) 114014.
[12] Y. Özüpak, S. Mansurov, A hybrid deep learning approach for multi-output short-term electricity demand forecasting, Concurr. Comput.: Pract. Exp. 37 (2025) e70356.
[13] B. Said, F.I. Bouguenna, Z. Ayyoub, M. Abdullah, Y. Özüpak, R. Bouddou, A. Soleimani, A. Pinnarelli, E. Aslan, I. Zaitsev, Hybrid MPC–Third-order sliding mode control with MRAS for fault-tolerant speed regulation of PMSMs under sensor failures, Int. Trans. Electr. Energy Syst. 2025 (2025) 5984024.
[14] A. Hornero, P.J. Zarco-Tejada, J.L. Quero, P.R.J. North, F.J. Ruiz-Gomez, R. Sanchez-Cuesta, R. Hernandez-Clemente, Modelling hyperspectral- and thermal-based plant traits for the early detection of Phytophthora-induced symptoms in oak decline, Remote Sens Env. 263 (2021) 112570.
[15] L. Tian, B. Xue, Z. Wang, D. Li, X. Yao, Q. Cao, Y. Zhu, W. Cao, T. Cheng, Spectroscopic detection of rice leaf blast infection from asymptomatic to mild stages with integrated machine learning and feature selection, Remote Sens Env. 257 (2021) 112350.
[16] J. Abdulridha, Y. Ampatzidis, S.C. Kakarla, P. Roberts, Detection of target spot and bacterial spot diseases in tomato using UAV-based and benchtop-based hyperspectral imaging techniques, Precis. Agric. 21 (2020) 955–978.
[17] R. Calderon, J.A. Navas-Cortes, C. Lucena, P.J. Zarco-Tejada, High-resolution airborne hyperspectral and thermal imagery for early, detection of verticillium wilt of olive using fluorescence, temperature and narrow-band spectral indices, Remote Sens Env. 139 (2013) 231–245.
[18] W. Huang, Q. Guan, J. Luo, J. Zhang, J. Zhao, D. Liang, L. Huang, D. Zhang, New optimized spectral indices for identifying and monitoring winter wheat diseases, IEEe J. Sel. Top. Appl. Earth. Obs. Remote Sens. 7 (2014) 2516–2524.
[19] L.Y. Liu, Y.Y. Dong, W.J. Huang, X.P. Du, B.Y. Ren, L.S. Huang, Q. Zheng, H.Q. Ma, A disease index for efficiently detecting wheat fusarium head blight using sentinel-2 multispectral imagery, IEEe Access. 8 (2020) 52181–52191.
[20] A.K. Mahlein, T. Rumpf, P. Welke, H.W. Dehne, L. Pluemer, U. Steiner, E.C. Oerke, Development of spectral indices for detecting and identifying plant diseases, Remote Sens Env. 128 (2013) 21–30.
[21] Y. Ren, H.C. Ye, W.J. Huang, H.Q. Ma, A.T. Guo, C. Ruan, L.Y. Liu, B.X. Qian, A new spectral index for the quantitative identification of yellow rust using fungal spore information, Big. Earth. Data 5 (2021) 201–216.
[22] M. Marshall, P. Thenkabail, T. Biggs, K. Post, Hyperspectral narrowband and multispectral broadband indices for remote sensing of crop evapotranspiration and its components (transpiration and soil evaporation), Agric. Meteorol. 218-219 (2016) 122–134.
[23] G.P. Asner, R.E. Martin, Spectral and chemical analysis of tropical forests: scaling from leaf to canopy levels, Remote Sens Env. 112 (2008) 3958–3970.
[24] J.B. Féret, A. Gitelson, S.D. Noble, S. Jacquemoud, PROSPECT-D: towards modeling leaf optical properties through a complete lifecycle, Remote Sens Env. 193 (2017) 204–215.
[25] J. Qi, D. Xie, T. Yin, G. Yan, J.-P. Gastellu-Etchegorry, L. Li, W. Zhang, X. Mu, L. K. Norford, LESS: largE-scale remote sensing data and image simulation framework over heterogeneous 3D scenes, Remote Sens Env. 221 (2019) 695–706.
[26] A. Damm, S. Cogliati, R. Colombo, L. Fritsche, A. Genangeli, L. Genesio, J. Hanus, A. Peressotti, P. Rademske, U. Rascher, D. Schuettemeyer, B. Siegmann, J. Sturm, F. Miglietta, Response times of remote sensing measured sun-induced chlorophyll fluorescence, surface temperature and vegetation indices to evolving soil water limitation in a crop canopy, Remote Sens Env. 273 (2022) 112957.
[27] T. Kattenborn, F.E. Fassnacht, S. Schmidtlein, Differentiating plant functional types using reflectance: which traits make the difference? Remote Sens. Ecol. Conserv. 5 (2019) 5–19.
[28] E. Osdaghi, A.J. Young, R.M. Harveson, Bacterial wilt of dry beans caused by Curtobacterium flaccumfaciens pv. flaccumfaciens: a new threat from an old enemy, Mol. Plant Pathol. 21 (2020) 605–621.
[29] J. Kuai, Y. Sun, M. Zhou, P. Zhang, Q. Zuo, J. Wu, G. Zhou, The effect of nitrogen application and planting density on the radiation use efficiency and the stem lignin metabolism in rapeseed (Brassica napus L.), Field. Crops. Res. 199 (2016) 89–98.
[30] Zhang, J., Pu, R., Huang, W., Yuan, L., Luo, J., Wang, J.J.F.C.R. (2012). Using in-situ hyperspectral data for detecting and discriminating yellow rust disease from nutrient stresses, 134, 165–174.
[31] A.D. Rocha, T.A. Groen, A.K. Skidmore, Spatially-explicit modelling with support of hyperspectral data can improve prediction of plant traits, Remote Sens Env. 231 (2019) 111200.
[32] C. Nie, L. Shi, Z. Li, X. Xu, D. Yin, S. Li, X. Jin, A comparison of methods to estimate leaf area index using either crop-specific or generic proximal hyperspectral datasets, Eur. J. Agron. 142 (2023) 126664.
[33] E.J. Botha, B. Leblon, B.J. Zebarth, J. Watmough, Non-destructive estimation of wheat leaf chlorophyll content from hyperspectral measurements through analytical model inversion, Int. J. Remote Sens. 31 (2010) 1679–1697.
[34] G.A. Blackburn, Relationships between spectral reflectance and pigment concentrations in stacks of deciduous broadleaves, Remote Sens Env. 70 (1999) 224–237.
[35] C.L. Brest, S.N. Goward, Deriving surface albedo measurements from narrow band satellite data, Int. J. Remote Sens. 8 (1987) 351–367.
[36] Z. Zhan, Q. Qin, A. Ghulan, D. Wang, NIR-red spectral space based new method for soil moisture monitoring, Sci. China D: Earth Sci. 50 (2007) 283–289.
[37] X. Chen, L. Vierling, D. Deering, A simple and effective radiometric correction method to improve landscape change detection across sensors and across time, Remote Sens Env. 98 (2005) 63–79.
[38] N. Leach, N.C. Coops, N. Obrknezev, Normalization method for multi-sensor high spatial and temporal resolution satellite imagery with radiometric inconsistencies, Comput. Electron. Agric. 164 (2019) 104893.
[39] H. Zhang, J. Li, Q. Liu, S. Lin, A. Huete, L. Liu, H. Croft, J.G. Clevers, Y. Zeng, X.J. M.i.E. Wang, A novel red-edge spectral index for retrieving the leaf chlorophyll content, Evolution 13 (2022) 2771–2787.
[40] S.M. Lundberg, S.-I.J.A.i.n.i.p.s. Lee, A unified approach to interpreting model predictions, Adv. Neural Inf. Process. Syst. 30 (2017) 4765–4774.
[41] A. Gitelson, M.N. Merzlyak, Spectral reflectance changes associated with autumn senescence of Aesculus hippocastanum L. and acer platanoides L. leaves. Spectral features and relation to chlorophyll estimation, J. Plant Physiol. 143 (1994) 286–292.
[42] A.A. Gitelson, A. Viña, V. Ciganda, D.C. Rundquist, T.J. Arkebauer, Remote estimation of canopy chlorophyll content in crops, Geophys. Res. Lett. 32 (2005) L08403.
[43] J. Dash, P. Curran, The MERIS terrestrial chlorophyll index, Int. J. Remote Sens. 25 (2004) 5403–5413.
[44] D. Haboudane, J.R. Miller, N. Tremblay, P.J. Zarco-Tejada, L. Dextraze, Integrated narrow-band vegetation indices for prediction of crop chlorophyll content for application to precision agriculture, Remote Sens Env. 81 (2002) 416–426.
[45] B. Datt, Visible/near infrared reflectance and chlorophyll content in Eucalyptus leaves, Int. J. Remote Sens. 20 (1999) 2741–2759.
[46] C. Wu, Z. Niu, Q. Tang, W. Huang, Estimating chlorophyll content from hyperspectral vegetation indices: modeling and validation, Agric. Meteorol. 148 (2008) 1230–1241.
[47] X. Liu, L. Liu, J. Hu, J. Guo, S. Du, Improving the potential of red SIF for estimating GPP by downscaling from the canopy level to the photosystem level, Agric. Meteorol. 281 (2020) 107846.
[48] J.A. Gamon, K.F. Huemmrich, C.Y.S. Wong, I. Ensminger, S. Garrity, D. Y. Hollinger, A. Noormets, J. Penuelas, A remotely sensed pigment index reveals photosynthetic phenology in evergreen conifers, Proc. Natl. Acad. Sci. U.S.A 113 (2016) 13087–13092.
[49] J. Penuelas, F. Baret, I. Filella, Semi-empirical indices to assess carotenoids/ chlorophyll a ratio from leaf spectral reflectance, Photosynthetica 31 (1995) 221–230.
[50] J.W. Rouse, R.H. Haas, J.A. Schell, D.W. Deering, Monitoring vegetation systems in the Great Plains with ERTS, NASA Spec. Publ. 351 (1974) 309.
[51] A.I. De Castro, R. Ehsani, R. Ploetz, J.H. Crane, J. Abdulridha, Optimum spectral and geometric parameters for early detection of laurel wilt disease in avocado, Remote Sens Env. 171 (2015) 33–44.
[52] A. Hornero, R. Hernandez-Clemente, P.R.J. North, P.S.A. Beck, D. Boscia, J. A. Navas-Cortes, P.J. Zarco-Tejada, Monitoring the incidence of Xylella fastidiosa infection in olive orchards using ground-based evaluations, airborne imaging spectroscopy and Sentinel-2 time series through 3-D radiative transfer modelling, Remote Sens Env. 236 (2020) 111480.
[53] A. Terentev, V. Dolzhenko, A. Fedotov, D. Eremenko, Current state of hyperspectral remote sensing for early plant disease detection: a review, Sensors 22 (2022) 757.
[54] N. Zhang, G. Yang, Y. Pan, X. Yang, L. Chen, C. Zhao, A review of advanced technologies and development for hyperspectral-based plant disease detection in the past three decades, Remote Sens. 12 (2020) 3188.
[55] K. Jomova, M. Valko, Health protective effects of carotenoids and their interactions with other biological antioxidants, Eur. J. Med. Chem. 70 (2013) 102–110.